Hamed Eghbali[1]
Wim De Malsche[1,2]
Jan De Smet[1]
Jeroen Billen[1]
Mauro De Pra[3]
Wim Th. Kok[3]
Peter J. Schoenmakers[3]
Han Gardeniers[2]
Gert Desmet[1]

[1]Department of Chemical Engineering, Vrije Universiteit Brussel, Brussel, Belgium
[2]Research Programme Mesofluidics, MESA+ Institute for Nanotechnology, MESA+ Research Institute, Enschede, The Netherlands
[3]Van't Hoff Institute for Molecular Sciences (HIMS), Universiteit van Amsterdam, Nieuwe Achtergracht, Amsterdam, The Netherlands

Original Paper

Experimental investigation of the band broadening originating from the top and bottom walls in micromachined nonporous pillar array columns

We report on the experimental investigation of the effect of the top and bottom wall plates in micromachined nonporous pillar array columns. It has been found that their presence yields an additional c-term type of band broadening that can make up a significant fraction of the total band broadening (at least if considering nonporous pillars and a nonretained tracer). Their presence also induces a clear (downward) shift of the optimal velocity. These observations are, however in excellent quantitative agreement with the theoretical expectations obtained from a computational fluid dynamics study. The presently obtained experimental results, hence, demonstrate that the employed high aspect ratio Bosch etching process can be used to fabricate micromachined pillar arrays that are sufficiently refined to achieve the theoretical performance limit.

Keywords: Band broadening / Computational fluid dynamics / Etched columns / On chip chromatography

Received: May 10, 2007; revised: July 6, 2007; accepted: July 6, 2007

DOI 10.1002/jssc.200700203

1 Introduction

In the past few years, more and more groups are trying to turn the micromachined column concept proposed in 1998 by Regnier and his group [1–3] into a practically useful alternative to the currently employed commercial capillary and narrow-bore HPLC columns. In this radically new approach to column manufacturing, the chromatographic support no longer consists of a packed bed of individual particles but instead consists of a regularly spaced array of photolithographically etched micropillars arranged on a silicon or glass substrate. As has been demonstrated theoretically in ref. [4–6], the perfect packing homogeneity that can be obtained using this manufacturing concept should allow to make a quantum leap in performance.

Experiments investigating the practical feasibility of micropillar array columns have been conducted by several groups in the past few years. Mogensen *et al.* [7] proposed a number of interesting fabrication strategies. He *et al.* [8] reported RP separations of FITC-tagged peptides in microfabricated columns in the CEC mode. In addition, Slentz *et al.* [3] investigated several COMOSS (collocated monolithic support structures) columns with varying dimensions. Working in the CEC mode as well, they were able to obtain an efficiency of 620 000 plates *per* metre using 10 μm deep channels filled with micromachined 'particles' of 5.2 × 5.2 μm (diamond shape).

Switching to pressure-driven flows, however, proved to be more difficult, partly because the pressure-driven flows are more sensitive to slight imperfections in the bed structure than electrically driven flows and partly also because the sealing between the top of the pillars and the cover plate becomes a more critical issue. Preliminary pressure-driven separations in nonporous pillar arrays have been presented by Ricoul *et al.* [9]. Recently, De Pra *et al.* [10] demonstrated reduced plate heights as low as 0.2 for a nonretained component in the pressure-driven mode, using an on-column injection system and excluding the extra band broadening originating from the sidewall zones. Using a similar device, our group succeeded very recently in performing the first high-performance liquid phase separations of a ternary mixture (plate heights of the order of 3 μm and a fastest separation time of 2.5 s) [11, 12].

Given that no theoretical expressions are available against which these measurements can be evaluated, it is however, not yet clear whether the achieved performances are near the theoretical limit or whether the tested columns are still underperforming. This is an important

Correspondence: Professor Gert Desmet, Department of Chemical Engineering (CHIS-IR), Vrije Universiteit Brussel, Pleinlaan 2, B-1050 Brussels, Belgium
E-mail: gedesmet@vub.ac.be
Fax: +32-2-6293248

Abbreviation: CFD, computational fluid dynamics

© 2007 WILEY-VCH Verlag GmbH & Co. KGaA, Weinheim

question because the number of problems that can prevent the achievement of the full theoretical potential of microfabricated pillar arrays is quite large. A first error source resides in the etching itself, for the exact desired shape and dimensions of the pillars and through pores cannot always be perfectly reproduced into the silicon or glass wafers. Also the slope of the sidewalls of the individual pillars can deviate from the desired perfectly vertical slope. In this case, the distance between the pillars will be larger near their top than near their bottom. In a pressure-driven flow, this will induce velocity differences extending over the depth of the channel which can in turn lead to some severe additional band broadening. Improper sealing of the channels and the inclusion of dust particles in the channels or between the cover plate and the pillar array are also certainly other major potential sources of imperfections. As are also the occurrence of specific adsorption events of the employed tracer molecules on the surface of the pillars, or the occurrence of additional band broadening in the employed in- and outlet channels or in the flow distribution regions.

Given this multitude of potential error sources, the present study aims at investigating how close the current state-of-the-art microfabrication techniques can approach the theoretically predicted performance. To determine these theoretical expectations, computational fluid dynamics (CFD) calculations have been used.

In a series of previous publications [4–6, 13, 14], our group has shown that CFD calculations are ideally suited to establish the theoretical performance limits of chromatographic supports. The commercial CFD software packages that exist nowadays allow solving the complete set of convection–diffusion equations determining the chromatographic performance in any given geometry and within a reasonable time. Dividing the flow domain into a sufficient number of computational grid cells, these calculations can be carried out with the highest possible precision. Studying a series of 2-D representations of pillar array columns, it was found that reduced plate heights as small as 0.07 should be possible under nonretentive conditions and with nonporous pillars, while minimal reduced plate heights between 0.7 and 1 (domain size reduced) were predicted under retentive conditions and with porous pillars, depending on the exact shape and positioning of the pillars [13]. In a later paper, still focussing on a 2-D representation of the pillar array, the additional band broadening originating from the channel sidewalls (Fig. 1) was analysed. It was found that an improper design of this sidewall region could lead to a dramatic plate height increase (easily up to a factor of 4) under nonretained conditions [15]. Fortunately, a simple redesign of the sidewall regions should be sufficient to completely remove this additional band broadening, at least under nonretained conditions and provided the fabrication accuracy is sufficient to yield the exactly desired dimensions for the pillar arrangement in the sidewall region. This issue has meanwhile been investigated and confirmed experimentally [10].

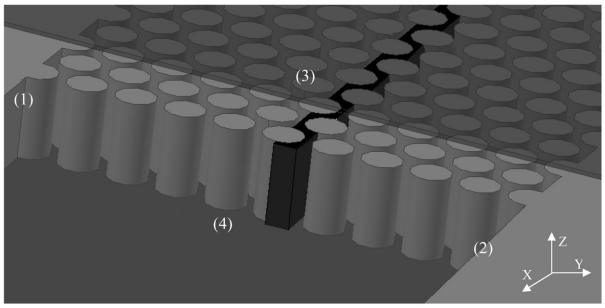

Figure 1. Drawing showing the cross-section of a pillar array column and identifying the two channel sidewalls (1) and (2) and the top (3) and bottom (4) walls that are needed to close off the micropillar array. The 3-D region coloured in black is the unit cell of the through pore system running through the cylinder arrays.

In a recent paper [16], the flow and dispersion in the complete 3-D structure of a pillar array column has been calculated to investigate how the presence of the top and bottom walls that are inevitably needed to close off the pillar array columns (Fig. 1) contribute to the total band broadening. In contrast with the sidewall effect, the additional band broadening originating from the top and bottom walls cannot be easily removed by a simple redesign of the wall zone. The top and bottom walls band broadening was found to display a large similarity with the additional band broadening originating from the two small sidewalls in an open-tubular channel, a problem that is well documented and understood [17]. The presence of the top and bottom walls was found to increase the minimal plate height of a nonporous pillar array from about $h = 0.07$ (hypothetical case without top and bottom walls) to $h = 0.16–0.18$, depending on the depth of the pillar array. The presence of the top and bottom walls was also found to reduce the optimal velocity (*i.e.* the velocity yielding the minimal plate height) for a nonretained component in the case of nonporous pillars ($\varepsilon = 40\%$) from $Pe = 70$ to $Pe = 20$. At velocities that are five times larger than the optimal velocity, the band broadening is increased with a factor of about 4 as compared to the hypothetical case without top and bottom walls.

In the present paper, this knowledge is used to evaluate the performance of a number of micropillar array channels that have been fabricated using the latest possibilities in photolithography and deep reactive etching. The band broadening originating from the sidewalls of the channels has been ruled out by measuring the band broadening only in the central portion of the channels. One of the motivations for the neglection of the sidewall effect, as already mentioned above, is that it can in prin-

© 2007 WILEY-VCH Verlag GmbH & Co. KGaA, Weinheim

ciple be completely eliminated (if the sidewall region is machined with a sufficient precision) and also because it has already been discussed elsewhere [10, 15]. Another reason to leave out the sidewall effect is that, since the effect is very sensitive to the smallest deviations from the ideal wall zone design [10, 15], it is very difficult to establish general conclusions about it.

2 Experimental

2.1 Channel fabrication

The pillar channels were defined in a silicon–glass sandwich. First, a 100 mm diameter (100) silicon wafer (*p*-type, 5–10 Ω · cm resistivity) was thermally (dry) oxidized at 1100°C until 200 nm silicon oxide was formed (Amtech Tempress Omega Junior). Then, normal UV photolithography (employed photoresist: Olin 907-12) was used to define the pillar arrays. Subsequently, the exposed silicon oxide was dry etched (Adixen AMS100DE, France), after which the resist was removed by oxygen plasma and nitric acid. Another lithography step was then used to define the inlet and outlet channels. The exposed silicon oxide was then etched and a Bosch-type deep reactive ion etch (Adixen AMS100SE) was used to make these channels 90 μm deep. After stripping the resist, another 10 μm was Bosch-etched into the exposed silicon, leaving pillars of 10 μm height and supply channels with a total depth of 100 μm. To remove the fluorocarbons, the wafers were set in an oxide furnace at 800°C for 30 min, after which the wafers were cleaned in nitric acid and dipped in HF. The top of the channels was formed by a 100 mm Pyrex® wafer. On the silicon wafer, through holes were first defined by photolithography on a dry resist foil (Ordyl BF410). The exposed glass was subsequently powder blasted using 30 μm alumina particles. After stripping the foil, the substrates were anodically bonded (voltage ramped to a maximum of 1000 V at 400°C, on an EVG EV-501 wafer bonder (EVGroup, Austria)).

In the design of the etching mask, each pillar was positioned on the grid points of a connected array of equilateral triangles. In the first channel (Fig. 2), the pillars had a target diameter of 5 μm (yielding an array of pillars with a mean diameter of 4.6 μm as measured by SEM after etching), and the side of each triangle was equal to 6.15 μm. With these data, it can be calculated that the external porosity (= relative interstitial volume) of this channel is equal to $\varepsilon = 49\%$. In the second investigated channel, the pillars had a centre-to-centre distance of 12.3 μm and a target diameter of 10 μm, finally resulting in 9.7 μm pillars after etching. With these data, the external porosity can be calculated to be given by $\varepsilon = 44\%$.

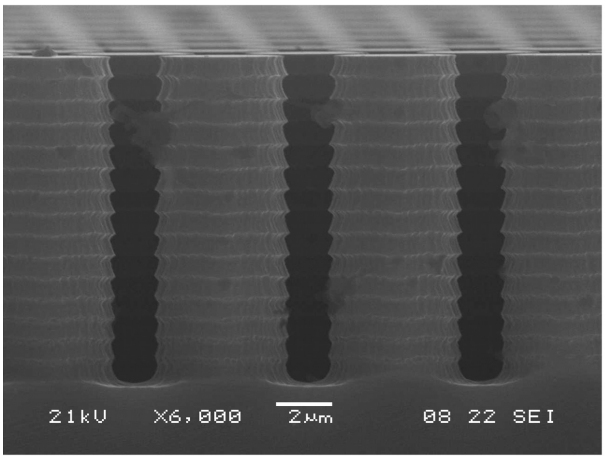

Figure 2. SEM image of micromachined pillars produced by the Bosch process on a silicon wafer. The indentations that can be observed on the walls of the pillars originate from the cyclic nature of the etching process.

2.2 System hardware

To connect the chip carrying the separations channels to the mobile phase and sample reservoirs, it was sandwiched between two homemade holders, of which the top one (made of PMMA) was perforated with drilled through holes that were compatible with the commercially available Nanoport™ connectors (Achrom, Belgium). The tubing used to connect the pump and the chip consisted of fused-silica capillaries (Achrom) with an id of 150 μm.

During the experiments, the chip was clamped onto the objective table of an inverted microscope (Axiovert 200, Zeiss NV, Belgium), equipped with a UV-1 filter cube set allowing for excitation at 350 nm and for emission above 450 nm. In this way, the standard Hg vapour lamp (HBO103/W2, Zeiss) of the microscope could be used to excite the fluorescent coumarin dyes in the UV. The maximal emission of the fluorescent light occured around 460 nm. The fluorescent plugs were visualized using an air-cooled CCD fluorescence camera (ORCA-ERC4742, Hamamatsu Photonics, Belgium) mounted on the video adapter of the microscope. The video images were subsequently analysed by the accompanying simple-PCI® 5.1 software. The microscope was mounted on a breadboard (M-IG 23-2, Newport, The Netherlands), together with a linear displacement stage (M-TS100DC.5, Newport) and a speed controller (MM, 4006 Newport). The displacement stage was used to translate the chip during the flow experiments. This allowed to keep the fluorescent plug in the field of view of the CCD camera over the entire channel length (5 cm) whilst being able to use a sufficiently high magnification zoom.

The sample reservoir as well as the mobile phase reservoir consisted of two different homemade stainless steel

© 2007 WILEY-VCH Verlag GmbH & Co. KGaA, Weinheim

vessels. These vessels were each connected to two different pressure controllers (EL-Press, Bronkhorst, The Netherlands), fed by a nitrogen gas bottle, that allowed to control the pressure in the vessels. This approach allowed applying two different independent pressure settings, one for the sample injection and the other for the mobile phase flow. The mobile phase pressure system was able to operate at pressures up to 25 bar. The two steps required for the injection of a plug could be successively executed by switching two external six-port valves (Rheodyne MX, Germany) at the same time.

2.3 Experimental conditions and procedures

The employed injection procedure has already been explained in great detail in ref. [11, 12]. In brief, the sample injection occurs on-chip by feeding the sample using a sideways oriented sample inlet and outlet channel into an injection zone devoid of pillars (200 μm wide in the present case). The injection procedure consists of two consecutive steps. During the first step, the mobile phase inlet and outlet are closed so that the only convective flow that can be generated goes from the sample inlet to the sample outlet, hence completely filling the (rectangular) injection zone. In the second step of the injection, both the sample inlet and outlet are closed (except for a small leakage flow that is needed to push the nonentered sample away from the injection zone) while the mobile phase inlet and outlet are opened to establish a mobile phase flow carrying the injected sample plug through the column.

All experiments were performed using a mobile phase composition of methanol–water (30:70 v/v). A phosphate buffer with pH = 7 was applied for the water phase. The employed nonretained sample solution consisted of a fluorescent dye, coumarin C480 (3×10^{-4} M) (Fluka, Belgium), dissolved in the same methanol–water (30:70 v/v) solution as that employed for the mobile phase. Prior to their use, all solutions were filtered (d_{por} = 0.2 μm) (Millipore, Belgium) in order to avoid blockage of the microchannels. Performing an open channel diffusion experiment as described in ref. [18], the molecular diffusivity of the coumarin dye was determined to be equal to 5×10^{-10} m^2/s in the employed methanol–water (30:70 v/v) mixture.

The plate height values (H) needed to assess the performance of the pillar arrays were determined from the difference between the spatial peak variance σ_x^2 measured in the video frame taken at the moment at which the peak was about 500 μm downstream of the injection zone and that measured in the video frame where the peak had already migrated a distance of about 1 cm, using

$$H = \frac{\Delta\sigma_x^2}{\Delta x} \quad (1)$$

wherein H (m) represents the absolute plate height, $\Delta\sigma_x^2$ (m^2) the difference in spatial peak variance and Δx (m) the migrated distance of the peak.

The spatial peak variances were determined using the Simple PCI software accompanying the employed CCD camera and translating the intensity of each individual pixel of the recorded image into an 8-bit light intensity value. To maximize the S/N ratio, the intensity values were averaged in the direction perpendicular to the mean flow. To exclude band broadening contributions coming from the high velocity region near the channel sidewalls, the average was restricted to the central rectangular part of the image, roughly 600 μm wide (see Fig. 3 for exact geometrical details). The average intensity values obtained for each vertical row of pixels were subsequently plotted *versus* the axial distance x and fitting these curves with a Gaussian peak profile (Fig. 3) using Sigma Plot, from which automatically a value for the best fitting spatial peak variance and the mean peak position was obtained. The latter was used to calculate the velocity of the peaks, using the time elapsed between the two analysed video frames.

2.4 Computational fluid dynamics simulations (CFD)

The computer simulations used in the present study have all been performed using a commercial CFD package (Fluent v6.1), allowing to solve the complete convection and diffusion species balances in complex flow domains. A CAD program (Gambit v2.3) was used to create a 2-D representation of the single flow-through pore depicted in Fig. 1. Applying 'symmetry' boundary conditions to the sides of this flow domain, it behaves as if it would be embedded in an infinitely wide array of pillars.

The same CAD program was also used as a grid generator to divide the flow domain into calculation cells. In the present case, the total flow domain consisted of 15 000 triangular grid cells, and a time step of 0.1 ms was used during the time-dependent solution of the mass balances. A second order upwind numerical discretization scheme (SIMPLE) was employed.

The procedures employed to derive the required peak moments and the concomitant plate height values from these simulations have already been abundantly described previously [4–6, 16] and are, therefore, not repeated here.

3 Results and discussion

Figures 3a and b show two CCD images of a sample plug migrating with a velocity of u = 0.50 mm/s, one taken

© 2007 WILEY-VCH Verlag GmbH & Co. KGaA, Weinheim

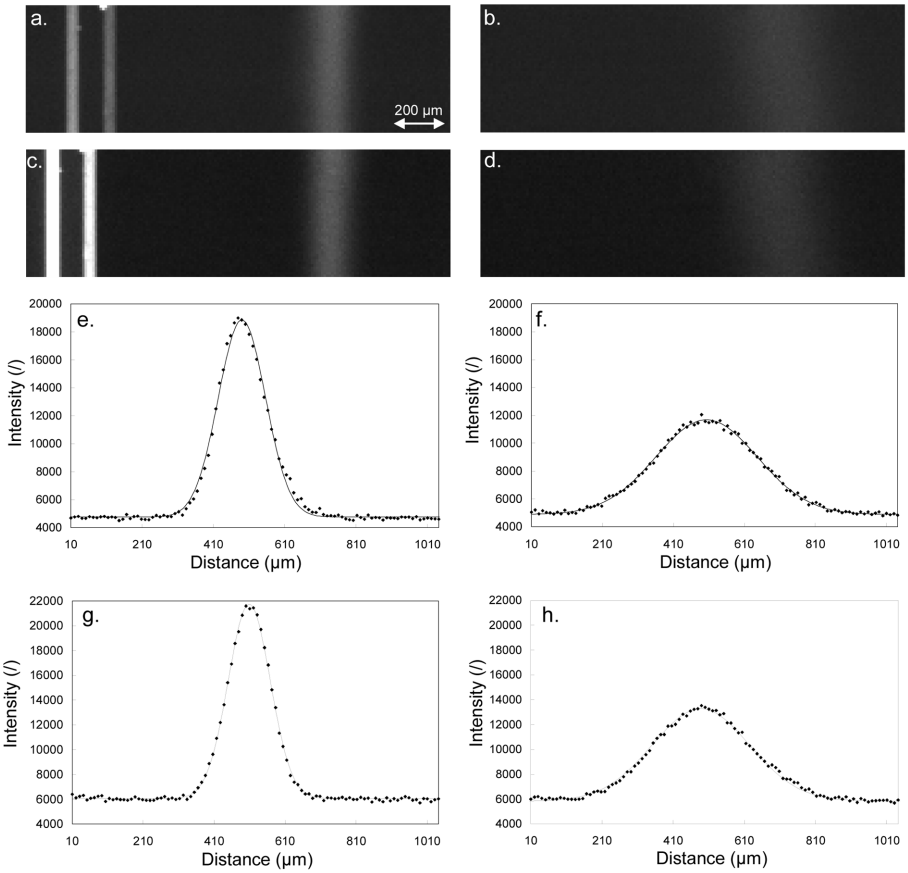

Figure 3. High resolution CCD images and intensity profiles of migrating peaks (nonretained component). (a, b) show the CCD images of a peak (u = 0.5 mm/s) just after injection and 1 cm downstream in the channel, while (e, f) show the concomitant intensity profiles. (c, d, g, h) relate to a similar experiment but now with a velocity of u = 2.86 mm/s.

shortly after the injection and the other taken 1 cm further downstream in the column. In Figs. 3c and d, two similar images are shown, but now for a sample plug migrating at a velocity of u = 2.86 mm/s. Below these images, the readout and the Gaussian fitting of the signals is given (Figs. 3e–h). As can be noted, the employed detection technique yields a very high S/N ratio and allows for a highly accurate determination of the peak shape. The comparison with the fitted Gaussian curve shows that the obtained bands are highly symmetrical and can be well fitted using

$$C = C_{\max} \exp\left(-0.5\left(\frac{x - x_0}{\sigma}\right)^2\right) \quad (2)$$

The distance of Δx = 1 cm elapsed by the sample plug between the two images used to calculate $\Delta\sigma_x^2$ was selected because it offered a good compromise between having a sufficient difference in spatial variance (to minimize the error on $\Delta\sigma_x^2$) on the one hand, while still giving a sufficiently high intensity to allow for an accurate determination of the concentration in the front and the tail of the peaks on the other hand. In a series of control experiments (varying Δx between 0.5 and 2 cm), it was checked that the obtained plate height values were independent of the employed Δx = 1 cm method.

The first video frame was always selected such that the peak centre was approximately at a position situated 500 µm downstream of the injector. This was done to ensure that the obtained plate height values only relate to the zone where the plate height contribution of the top and bottom walls has reached its constant, long time limit value. In ref. [16], it has been shown that the additional band broadening originating from the top and bottom walls goes through a transient regime. Depending on the depth of the channel (d = 12 µm in the present case) and the employed liquid velocity this transient regime covers the initial range of 20–100 µm of the channel (cited values are for a mobile phase velocity u of respectively 3 and 14 mm/s). Both values are clearly smaller than the 500 µm 'safety margin' that has been respected in the present study to measure the first peak profile.

The origin of the transient plate height regime can best be understood on the basis of the flow field that is established in the through pores of the cylinder array. In ref. [16], it has been shown that this flow field displays a very large similarity with the flow through an open-tubular channel with a constant, flat rectangular crosssection. Trying to visualize this similarity and referring to the schematic array representation shown in Fig. 1, one

© 2007 WILEY-VCH Verlag GmbH & Co. KGaA, Weinheim

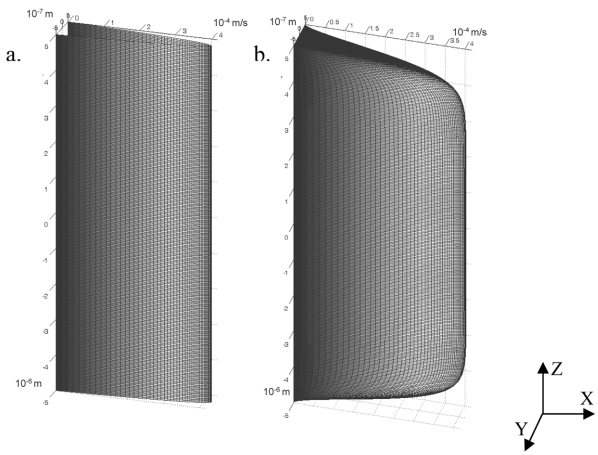

Figure 4. 3-D representation of the flow profile within a flat rectangular channel (a) without and (b) with top and bottom effect. The velocity field for the latter case has been calculated from Eq. (3) with $\Delta P = 10$ bar, $\eta = 10^{-3}$ Pa · s, $d = 1$ μm, $w = 10$ μm and $L = 30$ cm.

should consider a rectangular channel having its two long walls running in the *z*-direction and having its two short sidewalls coinciding with the small parts of the top and bottom wall plates that are in contact with the liquid in an individual through pore.

Figure 4a shows the flow field in a (hypothetical) flat rectangular channel having no short sidewalls, *i.e.* one that extends over an infinitely wide distance. In this case, the flow field is parabolic in the *y*-direction and flat in the *z*-direction. As depicted in Fig. 4b, the flow arresting effect of the two short sidewalls (in the present case corresponding to the top and bottom plates) creates a flow field wherein the central portion is still identical to the flow in the sidewall less case, while the velocity drops to zero in two zones with a thickness of the order of $d/2$ close to the short sidewalls (d is the width of the rectangle).

The flow field shown in Fig. 4b is well established and can be analytically calculated using [19]

$$u(z,y) = \frac{\Delta P}{2\eta L}\left(\frac{d^2}{4} - y^2\right) - \frac{4\Delta P d^2}{\eta L \pi^3} \sum_{n=1,3,5\ldots}^{+\infty} \frac{1}{n^3} \sin \left(\frac{n\pi}{d}\left(y + \frac{d}{2}\right)\right) \frac{\cos h\left(\frac{n\pi z}{d}\right)}{\cos h\left(\frac{n\pi w}{2d}\right)} \quad (3)$$

The band broadening arising from the parabolic velocity profile in the *y*-direction is incorporated in the 2-D band broadening plate height values ($H_{2\text{-D}}$) that are obtained if computing the band broadening in a 2-D array of cylinders, as was done in the CFD studies reported in ref. [4–6, 13–15]. The presence of the low velocity regions near the two short sidewalls in the case of 3-D case inevitably induces an additional band broadening that is not accounted for in the 2-D solution, because in the 3-D case the equilibration between the different velocity lines not only has to occur in the *y*-direction but also in the *z*-direction.

In an open-tubular channel, this additional band broadening process is well understood [20–24]. During the first moments of this dispersion process, not all species have already experienced the presence of the slower moving zone so that most of them still only experience the basic 2-D band broadening originating from the velocity gradient in the *y*-direction. As the time proceeds, progressively more and more species are being exchanged (through the process of molecular diffusion) with the slower moving sidewall zones, and are hence being influenced by this additional source of band broadening. As a result, the ensemble averaged band broadening increases with time. This continues until all molecules have been exchanged at least once with the sidewall zones (top and bottom walls in the case of the presently considered pillar array). Once this is the case, the plate height reaches a constant, long time-limit value.

Figure 5 shows the measured (long time limit) plate heights as a function of the mobile phase velocity. One series of data points (for the 10 μm pillar channel) were already reported in a previous study [10]. The range of velocities that was accessible in this experiment was too small to enter quite deeply into the c-term of the Van Deemter curve. For the 5 μm pillar channel, tested with a newer setup, significantly higher velocities could be obtained, allowing to enter the c-term dominated regime of the Van Deemter curve.

It is very interesting to note from a practical point of view that the plate heights near the minimum of the Van Deemter curve under the presently considered nonretained component conditions are as low as 1 μm, whereas a packed column with the same pillar size (5 μm) would rather have a minimal plate height of $H_{min} = 10$ μm, if using the generally accepted packed bed rule that $h_{min} \cong 2$ [24]. Also, the plate heights in the c-term dominated regime are very low and increase much more slowly with u than is the case in a packed column.

A good test to investigate the quality of chromatographic data obtained in systems with a different size is to switch to the reduced parameter representation originally introduced by Giddings [25], using $h = H/d_p$ and $\nu = u d_p/D_m$. As can be noted from Fig. 6, this indeed allows to bring the 5 and the 10 μm pillar data into close agreement. The agreement is, however, not perfect. Besides possible influences of measurement errors, one of the reasons for the lack of a really perfect agreement needs to be found in the underetching problem.

This underetching problem, leading to pillars that are some 200–400 nm smaller than the size they had on the

© 2007 WILEY-VCH Verlag GmbH & Co. KGaA, Weinheim

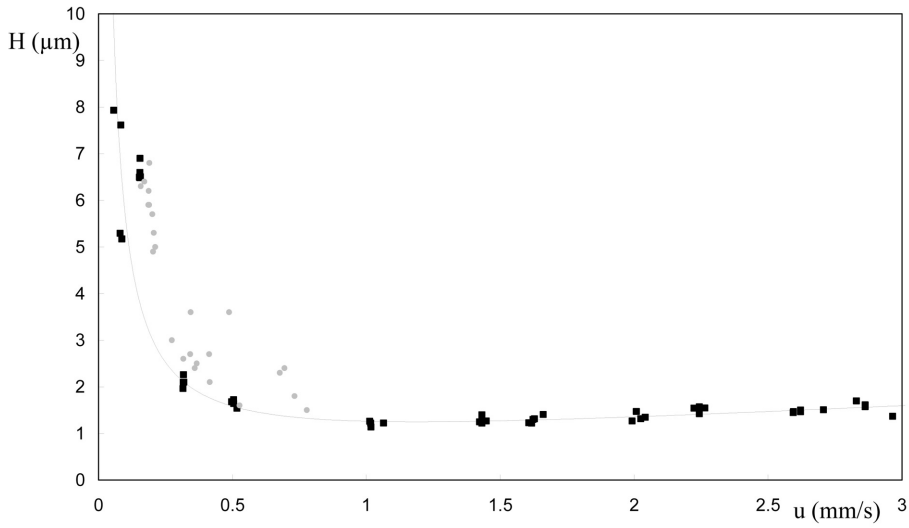

Figure 5. Plot of plate height (*H*) *versus* velocity (*u*) of two pillar array columns with different pillar array diameter. The experimental data for the 5 μm pillars (black squares) were shown with their best curve fit with Eq. (4), yielding by $a = 0.01$, $b = 1.47$ and $c = 0.0091$ (full line curve). The experimental data for the 10 μm pillars (grey dots) have already been shown in [10].

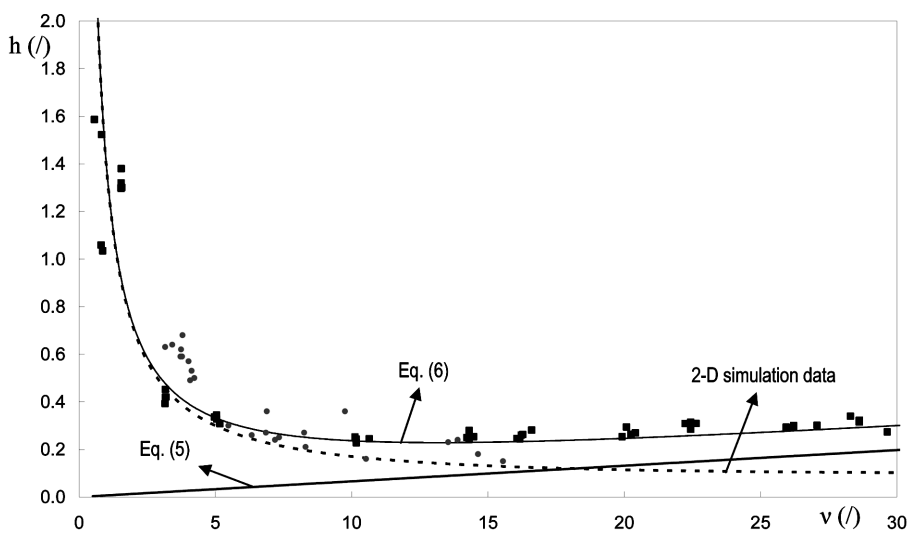

Figure 6. Plot of reduced plate height (*h*) *versus* reduced velocity (ν). The black squares represent the same experimental 5 μm pillar data as in Fig. 5. The dashed line curve represents the plate height values ($h_{2\text{-D}}$) that would be obtained without top and bottom walls (pure 2-D case, data generated using CFD calculations). The grey line represents the separate plate height contribution of the top and bottom walls (h_{tb}) detemined by Eq. (5), while the full line curve shows the sum ($h_{2\text{-D}} + h_{tb}$) of the two previously mentioned contributions.

original mask, is an inevitable problem with the current generation of high-aspect ratio etchers. As a result of this underetching, the external porosity of the pillar arrays is always slightly larger than the original design imprinted on the etching mask. In the present case, the underetch yielded 4.6 μm pillars instead of the envisioned 5 μm pillars (leading to an external porosity $\varepsilon = 49\%$ instead of the originally targeted 40%), whereas the nominal 10 μm pillars in reality had a diameter of approximately 9.7 μm (leading to an external porosity of $\varepsilon = 44\%$). In principle, the underetching error can be removed by going through a succession of optimization steps (drawing oversized pillars in the mask to compensate for the anticipated underetching), but this process requires at least two or three iterations and is hence very expensive.

Given that the 5 μm pillar array is proportionally more affected by the underetching problem than the 10 μm pillar array and hence also has a slightly larger external porosity, both arrays are no longer perfectly geometrically similar, a *conditio sine qua non* to obtain a perfect overlap in the reduced plate height representation [25, 26]. Nevertheless, the 5 and 10 μm curves overlap quite well in Fig. 6, so that it can be concluded that the influence of this difference in external porosity is rather small.

Fitting the 5 μm pillar data series with the basic Van Deemter expression [27, 28]

$$h = a + b/\nu + c\nu \tag{4}$$

a good fit of the experimental data could be obtained. To avoid overloading Fig. 6, the fitted curve has been added to Fig. 5, after transforming the reduced plate height values into absolute plate height values. The best fitting parameters were found to be given by $a = 0.01$, $b = 1.47$ and $c = 0.0091$. Both *a* and *c*-values are much smaller than that in a packed column, clearly reflecting the advantage

© 2007 WILEY-VCH Verlag GmbH & Co. KGaA, Weinheim

of a perfectly ordered pillar array column. A moderating remark about the small c-value is that this small value is especially due to the fact that nonporous pillars are considered. If porous pillars would have been used, the c-term constant certainly would have been significantly larger.

Figure 6 shows the reduced plate height curve (dashed curve) for a nonretained component that would be obtained in perfectly ordered 2-D array with the same 50% external porosity as the 5 μm pillar array tested experimentally. These 2-D array data have been generated numerically using the CFD routine described in the Section 2.

Fitting these 2-D data with Eq. (4), the best fit is obtained for $a = 0.004$, $b = 1.47$ and $c = 0.001$. Comparing these values with the a, b and c-values obtained for the experimental data fit shown in Fig. 5, the main difference between the 2-D and the 3-D case clearly is to be found in the c-term band broadening (about nine times larger experimentally in 3-D than in the numerical 2-D model).

The latter is in full agreement with our recent result from theoretical study about the additional contribution of the presence of top and bottom plates on the band broadening in a micropillar array column. In ref. [16], the similarity between the flow through the pores of a micromachined pillar array and the flow through a flat rectangular open channel already referred to during the discussion of Fig. 4 has been used to show that this contribution is of the c-term type, *i.e.* linearly proportional with the mobile phase velocity. Using the similarity between both flow types, it was possible to establish a correlation for this additional plate height contribution (H_{tb})

$$H_{tb} = \frac{\kappa_{Aris} u d_{por}^2}{2D_m} \quad (5)$$

In Eq. (5) which was misprinted in ref. [16], u is the linear velocity, D_m the molecular diffusivity, κ_{Aris} a dimensionless constant and d_{por} is a characteristic pore size, which was defined in ref. [16] as d_{wall}. In contrast to what might be expected based on the fact that it originates from a velocity difference in the z-direction, the H_{tb}-value depends in most practical cases especially on the width of the flow through pores (d_{por}, measured in the y-direction) and only to a much smaller extent on the depth w of the pores (w is measured in the z-direction), hence the explicit appearance of d_{por} in the expression for H_{tb}.

The influence of the pore depth w only appears in the value of κ_{Aris}, a geometrical constant originally introduced by Aris [17] to describe the sidewall induced band broadening in open-tubular flat rectangular channels. The value of this constant varies more or less linearly with the pore aspect ratio (w/d_{por}) if w/d_{por} is roughly smaller than 4. For large values of w/d_{por} (*i.e.* for $w/d_{por} \gg 10$), κ_{aris} becomes nearly completely independent of w/d_{por} and approaches a constant value ($\kappa_{Aris} = 0.13$). A complete representation of how κ_{Aris} exactly varies with w/d_{por} can be found in ref. [16, 29].

Considering the exact dimensions of the presently considered 5 μm pillar array, for which the channel depth and the characteristic pore size were respectively equal to $w = 12$ μm and $d_{por} = 1.63$ μm, the w/d_{por} aspect ratio has a value of 7.36. As can be noted from the data given in ref. [16, 29], the κ_{Aris}-value corresponding to this value is given by $\kappa_{Aris} = 0.103$. Using this value, the reduced plate height variant of Eq. (5) can be readily calculated. The result of this calculation, a straight line passing through the origin, has been added to Fig. 6 (grey coloured line).

The theory of the sidewall band broadening in open-tubular channels also shows that the 2-D and the sidewall contributions are simply additive [17, 29] provided the aspect ratio of the channels is sufficiently large. Translated in terms of the cylindrical pillar array, this means that the h_{tb}-contribution can be simply added to the 2-D plate height values to obtain the total band broadening for the 3-D system

$$h_{3-D} = h_{2-D} + h_{tb} \quad (6)$$

provided the distance between the pillars is at least about 5–10 times smaller than the height of the pillars.

Applying Eq. (6), and adding the h_{tb}-contribution determined by Eq. (5) to the $h_{2\text{-}D}$-data represented by the dashed line curve shown in Fig. 6, the full black line is obtained. The excellent agreement between this theoretical curve and the experimental data not only validates Eqs. (5) and (6) and the theoretical calculations presented in ref. [16], but also shows that the presently employed microfabrication method is sufficiently accurate to achieve the very low plate heights that are theoretically possible with a perfectly ordered micropillar array. This also means that the presence of the undulations or scallops that can be noted on the outer surface of the pillars (*cf.* Fig. 2), and that are caused by the cyclic nature of the employed etching process, has no significant influence on the band broadening.

4 Concluding remarks

Assessing the quality of a micromachined nonporous pillar array column using a nonretained marker, the band broadening originating from the top and bottom walls cannot be neglected. The presence of the top and bottom walls gives rise to a contribution that increases linearly with the applied velocity (Pe-number). The exact extent of this contribution depends on the pillar height and the interpillar distance and hence has to be calculated case *per* case. For a pillar array with external porosity $\varepsilon = 50\%$ and with a ratio of pillar height to interpillar distance

© 2007 WILEY-VCH Verlag GmbH & Co. KGaA, Weinheim

equalling about a factor of 7, the top and bottom walls induced band broadening makes up about 30% (at Pe = 10) to 65% (at Pe = 30). It also shifts the optimal operating velocity from a value of Pe = 40 (hypothetical 2-D case without top and bottom walls) to a value of Pe = 10.

Making the necessary top and bottom walls band broadening correction, the present study has demonstrated that it is currently possible to fabricate micromachined pillar arrays with such a high precision that they yield plate heights that are as small as theoretically predicted, at least if the sidewall effect is excluded. This observation however only holds for 5 and 10 μm pillar arrays. The next step in the present study is now to use advanced lithographic etching techniques to investigate whether it is still possible to produce pillar arrays with smaller pillar diameters (*e.g.* in the 1 – 3 μm range) but with the same high etching accuracy as the currently investigated 5 and 10 μm pillar arrays.

H. E. is supported through a grant from the Flemish Fund for Scientific Research of the Belgian Government (FWO-Vlaanderen). D. Clicq is Postdoctoral Fellow of the same institute (FWO-Vlaanderen).

Symbols

a, b, c terms in the Van Deemter equation (Eq. 4) (/)
C detector signal (/)
C_{max} maximal detector signal (/)
d pore width (m)
D_m molecular diffusion constant (m^2/s)
d_p pillar diameter (m)
d_{por} pore diameter (m)
h reduced plate height (/)
H plate height (m)
$h_{3\text{-}D}$ 3-D plate height estimation ($h_{2\text{-}D} + h_{tb}$) (/)
$H_{2\text{-}D}$ plate height from 2-D CFD simulations (m)
h_{tb} top and bottom cover plate contribution to band broadening (/)
L channel length (m)
x longitudinal position (m)
y radial position (m)
x_0 peak position (m)
u linear velocity (m/s)
w pore depth (m)

Greek symbols

ε porosity (/)
Δx longitudinal distance (m)
ΔP pressure drop (Pa)
η viscosity (Pa.s)
κ_{aris} Aris constant, dependant on geometry and flow profile (/)
ν reduced velocity (Peclet number) (/)
σ_x^2 spatial peak variance (m^2)

5 References

[1] He, B., Regnier, F., *J. Pharm. Biomed. Anal.* 1998, *17*, 925 – 932.
[2] Regnier, F., *J. High Resolut. Chromatogr.* 2000, *23*, 19 – 26.
[3] Slentz, B. E., Penner, N. A., Lugowska, E., Regnier, F., *Electrophoresis* 2001, *22*, 3736 – 3743.
[4] Gzil, P., Vervoort, N., Baron, G. V., Desmet, G., *Anal. Chem.* 2003, *75*, 6244 – 6250.
[5] Gzil, P., Vervoort, N., Baron, G. V., Desmet, G., *Anal. Chem.* 2004, *76*, 6707 – 6718.
[6] De Smet, J., Gzil, P., Vervoort, N., Verelst, H., Baron, G. V., Desmet, G., *Anal. Chem.* 2004, *76*, 3716 – 3726.
[7] Mogensen, K. B., Eriksson, F., Gústafsson, O., Nikolajsen, R. P. H., Kutter, J. P., *Electrophoresis* 2004, *25*, 3788 – 3795.
[8] He, B., Ji, J., Regnier, F., *J. Chromatogr. A* 1999, *853*, 257 – 262.
[9] Ricoul, F., Bouffet, S., Sarrut, N., Mittler, F., Constantin, O., Blanc, R., Sudor, J., Vinet, F., Garin, J., Vauchier, C., *29th International Symposium on High Performance Liquid Phase Separations and Related Techniques* 2005 June, Stockholm-Sweden, pp. 26 – 30.
[10] De Pra, M., Kok, W. Th., Gardeniers, J. G. E., Desmet, G., Eeltink, S., van Nieuwekasteele, J. W., Schoenmakers, P. J., *Anal. Chem.* 2006, *78*, 6519 – 6525.
[11] Eghbali, H., De Malsche, W., Clicq, D., Gardeniers, H., Desmet, G., *LC GC Eur.* 2007, *20*, 208 – 222.
[12] De Malsche, W., Eghbali, H., Clicq, D., Vangelooven, J., Gardeniers, H., Desmet, G., *Anal. Chem.* 2007, *79*, 5915 – 5926.
[13] De Smet, J., Gzil, P., Vervoort, N., Verelst, H., Baron, G. V., Desmet, G., *J. Chromatogr. A* 2005, *1073*, 43 – 51.
[14] Gzil, P., De Smet, J., Desmet, G., *J. Sep. Sci.* 2006, *29*, 1675 – 1685.
[15] Vervoort, N., Billen, J., Gzil, P., Baron, G. V., Desmet, G., *Anal. Chem.* 2004, *76*, 4501 – 4507.
[16] De Smet, J., Gzil, P., Vervoort, N., Verelst, H., Baron, G. V., Desmet, G., *J. Chromatogr. A* 2007, *1154*, 189 – 197.
[17] Aris, R., *Proc. R. Soc.* 1956, *A235*, 67 – 77.
[18] Pappaert, K., Biesemans, J., Clicq, D., Vankrunkelsven, S., Desmet, G., *Lab Chip* 2005, *10*, 1104 – 1110.
[19] Schlichting, H., *Boundary-Layer Theory*, McGraw Hill, London 1958.
[20] Golay, J. E., *J. Chromatogr.* 1981, *216*, 1 – 8.
[21] Doshi, M. R., Daiya, P. M., Gill, W. N., *Chem. Eng. Sci.* 1978, *33*, 795 – 804.
[22] Dutta, D., Leighton, D. T., Jr., *Anal. Chem.* 2001, *73*, 504 – 513.
[23] Desmet, G., Baron, G. V., *J. Chromatogr. A* 2002, *946*, 51 – 58.
[24] Poppe, H., *J. Chromatogr. A* 2002, *948*, 3 – 17.
[25] Giddings, J. C., *Dynamics of Chromatography – Part I*, Marcel Dekker, New York 1965.
[26] Billen, J., Gzil, P., Baron, G. V., Desmet, G., *J. Chromatogr. A* 2005, *1077*, 28 – 36.
[27] Van Deemter, J. J. V., Zuiderweg, F. J., Klinkenberg, A., *Chem. Eng. Sci.* 1956, *5*, 271 – 289.
[28] Neue, U., *HPLC Columns. Theory, Technology and Practice*, Wiley-VCH, New York 1997.
[29] Cifuentes, A., Poppe, H., *Chromatographia* 1994, *39*, 391 – 404.

© 2007 WILEY-VCH Verlag GmbH & Co. KGaA, Weinheim